Full length article

Strain-induced martensite decay in bearing steels under rolling contact fatigue: Modelling and atomic-scale characterisation

CrossMark

Hanwei Fu [a], Wenwen Song [b], Enrique I. Galindo-Nava [a],
Pedro E.J. Rivera-Díaz-del-Castillo [c, *]

[a] Department of Materials Science and Metallurgy, 27 Charles Babbage Road, University of Cambridge, CB3 0FS UK
[b] Steel Institute (IEHK), RWTH Aachen University, Germany
[c] Department of Engineering, Engineering Building, Lancaster University, LA1 4YW UK

A B S T R A C T

Martensite decay in bearing steels manifested as dark etching regions (DERs) under rolling contact fatigue (RCF) is modelled. The proposed model is established based on a dislocation-assisted carbon migration mechanism. The proposed model is capable of predicting the progress of DER formation and the corresponding mechanical property evolution with increasing number of cycles, in good agreement with the experimental data reported throughout seventy years. The effects of RCF testing conditions on DER formation are studied and a useful tool, DER% maps, is developed for illustrating the temperature, contact pressure and number of cycles for DER occurrence. Moreover, an atom probe tomography study is carried out, revealing the nature of DER ferrite and obtaining strong evidence supporting the postulated DER formation mechanism. The successful application of the dislocation assisted carbon migration mechanism to DER formation provides a plausible explanation to the phenomenon of martensite decay under rolling contact fatigue.

1. Introduction

Bearings are important engineering components to deliver rotational loads. High carbon martensitic steels are most frequently used for bearing applications to meet harsh serving environments, including high contact pressures, high rotational speeds and sometimes elevated temperatures [1]. However, after a high number of stress cycles, microstructural alterations occur in the material, signalling the onset of rolling contact fatigue (RCF) [2,3]. One of the key microstructural alterations is the decay of martensite manifested as dark etching regions (DERs). DERs are formed at the subsurface of bearing inner rings, and the occurrence of DERs is an implication of microstructural instability [4]. As the name indicates, DERs display a dark contrast under optical microscopy (OM) after etching with nital when they are studied in either the axial section or the circumferential section of a fatigued bearing inner ring (Fig. 1(a)). Fig. 1(b) shows a DER observed in the axial section. The formation of DERs is detrimental as the resultant microstructure

exhibits lower hardness than the parent martensite [5–11] and consequently becomes less resistant to cyclic loading.

First observed by Jones in 1946 [12], the microstructure of DERs was described as "mechanical troostite", which was later confirmed to be ferrite by electron diffraction analysis [13–15]. Actually, a DER consists of dark patches distributed in the parent martensite matrix, with the former gradually consuming the latter with increasing the number of stress cycles. Given that the solubility of carbon in ferrite is only 0.02 wt% [16], the question arises as to the whereabouts of the excess carbon when such martensite-ferrite transformation occurs. Therefore, describing the carbon redistribution process during DER formation becomes the key to understanding such martensite decay. Although having been discussed for several decades, a plausible formation mechanism for DERs is still unavailable. Some authors [5,6] argued that DERs formation results from the over-tempering of martensite, and the fact that DERs have never been observed in the fatigued bearing samples initially tempered to a hardness of around 700 HV [13,17] supports this argument. However, the operation temperatures of bearings, which are usually lower than 100 °C, are not sufficiently high to thermally activate the growth of carbides [18], and there is no evidence showing distinct temperature rise in DERs caused by cyclic
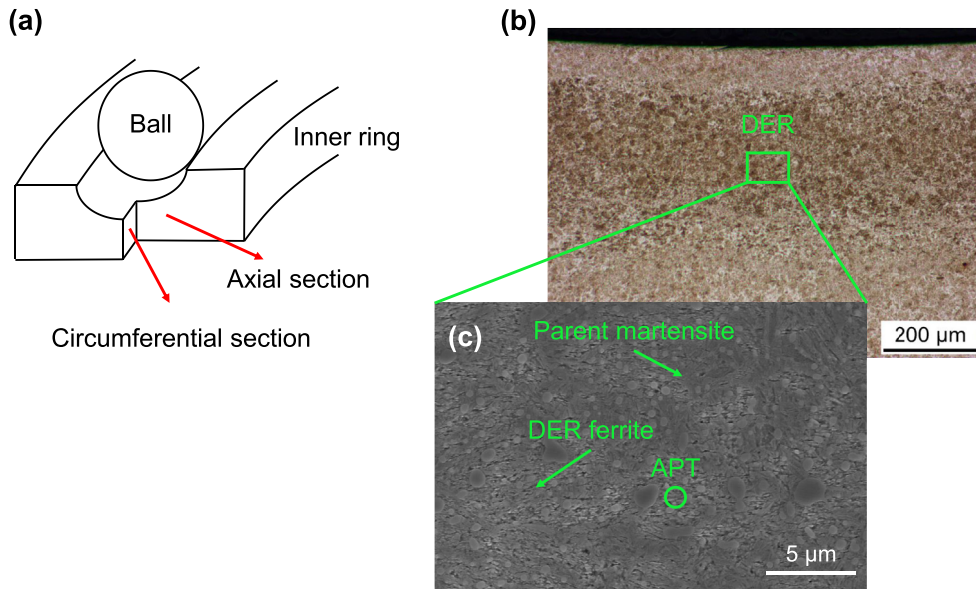
Fig. 1. (a) Schematic showing the circumferential and axial sections of a bearing inner ring. (b) OM image of a DER observed from the axial section. (c) Secondary electron (SE) image of the DER showing the location where the APT specimen was prepared.

stressing. Besides, Bush et al. [5] found threshold contact pressures below which DERs were never formed, indicating the essential role played by stress. Moreover, the depth range where a DER is formed is considered to be related to the stress state of Hertzian contact, although there is still in disagreement as to the stress component responsible for such phenomenon with some authors [15,19] arguing it is the maximum shear stress, others [13,20] that it is the 45° shear stress, the orthogonal shear stress [5,6] or the von-Mises stress [9]. Nevertheless, it was experimentally proved [15] that increasing either contact pressure or operation temperature can accelerate DER formation. As for the carbon distribution in DERs, Swahn et al. [8] postulated that the excess carbon resides at dislocations and the cyclic stress somehow promotes the carbon migration, but this requires an unrealistically high dislocation density of 10^{17} m^{-2} contradicting the observation of hardness decrease in DERs, which apparently implies a carbon depletion in the matrix. Recently, Kang et al. [19] postulated a more plausible mechanism, stating that during DER formation the excess carbon migrates to pre-existing carbide precipitates with the assistance of gliding dislocations thickening them; the model managed to explain the material softening in DERs but failed to accurately describe the effects of temperature, rotational speed and contact pressure. In this context, a dislocation-assisted carbon migration theory was suggested by a recent study [21] to describe the precipitation of lenticular carbides (LCs) in rolling contact fatigued bearing steels, which can also be applied to describe the thickening of pre-existing carbide precipitates in DERs.

In this work, a novel DER formation model is established based on the dislocation assisted carbon migration theory, and the predicted results are compared with experimental measurements from both this research and the literature. As for the characterisation of DERs, studies [22,23] on white etching areas have shown atom probe tomography (APT) to be a powerful tool to reveal carbon redistribution in rolling contact fatigued bearing steels. Therefore, APT is also performed on DER ferrite specimens.

2. DER formation model

Prior to RCF testing, the initial microstructure of bearing steels,

as schematically illustrated in Fig. 2 (c), is tempered martensite, containing a large amount of nano-sized precipitates, namely temper carbides, evenly distributed within a martensitic matrix supersaturated with carbon [24]. Hence, from a thermodynamic point of view, carbon in solid solution tends to migrate towards the precipitates for their further growth, but the kinetics are suppressed at usual bearing operation temperatures due to insufficient carbon diffusivity. However, this process can be reactivated if a dislocation-assisted carbon flux is present. It is believed that the microstructural alterations in bearing steels occur at the plastic shakedown stage of RCF where a steady state plastic flow is present [25]. According to the analysis in Ref. [21], gilding dislocations can drag the Cottrell atmospheres formed around them and generate a carbon flux owing to the unique stress history of rolling contact. Such dislocation-assisted carbon flux is schematically shown in Fig. 2 (a) and (b), where the time interval t_c between neighbouring stress pulses allows for carbon to migrate back towards those dislocations that just moved for ΔL to form Cottrell atmospheres. The magnitude of such carbon flux (J_d), referring to [21], is given by:

$$J_d = \frac{\Delta\gamma\dot{N}}{b}\left[3\left(\frac{\pi}{2}\right)^{\frac{1}{3}}\left(\frac{AD}{kT\dot{N}}\right)^{\frac{2}{3}}C_{Vm}\right],\qquad(1)$$

where $\Delta\gamma$ denotes the plastic shear strain amplitude within each stress cycle, $\dot{N}$ denotes the rotational speed, b denotes the magnitude of Burgers vector, A denotes the interaction energy between a carbon atom and a dislocation strain field, D denotes the diffusion coefficient of carbon atoms in body-centred cubic iron, k denotes the Boltzmann constant, T denotes the temperature and C_{Vm} denotes the carbon concentration in the matrix per unit volume.

The dislocation assisted carbon flux can contribute to the kinetics of precipitate thickening, leaving a carbon depleted matrix which eventually transforms into DER ferrite. Hence a DER formation model can be established. As shown in Fig. 2 (d), a temper carbide is taken as a thin plate with a half width r_p. This morphology was detected by transmission electron microscopy [24,26] and was used in previous modelling work on bearing steels [19]. The carbide precipitate can be thickened from its both sides, and thereby at the proceeding interface on each side, a carbon flux
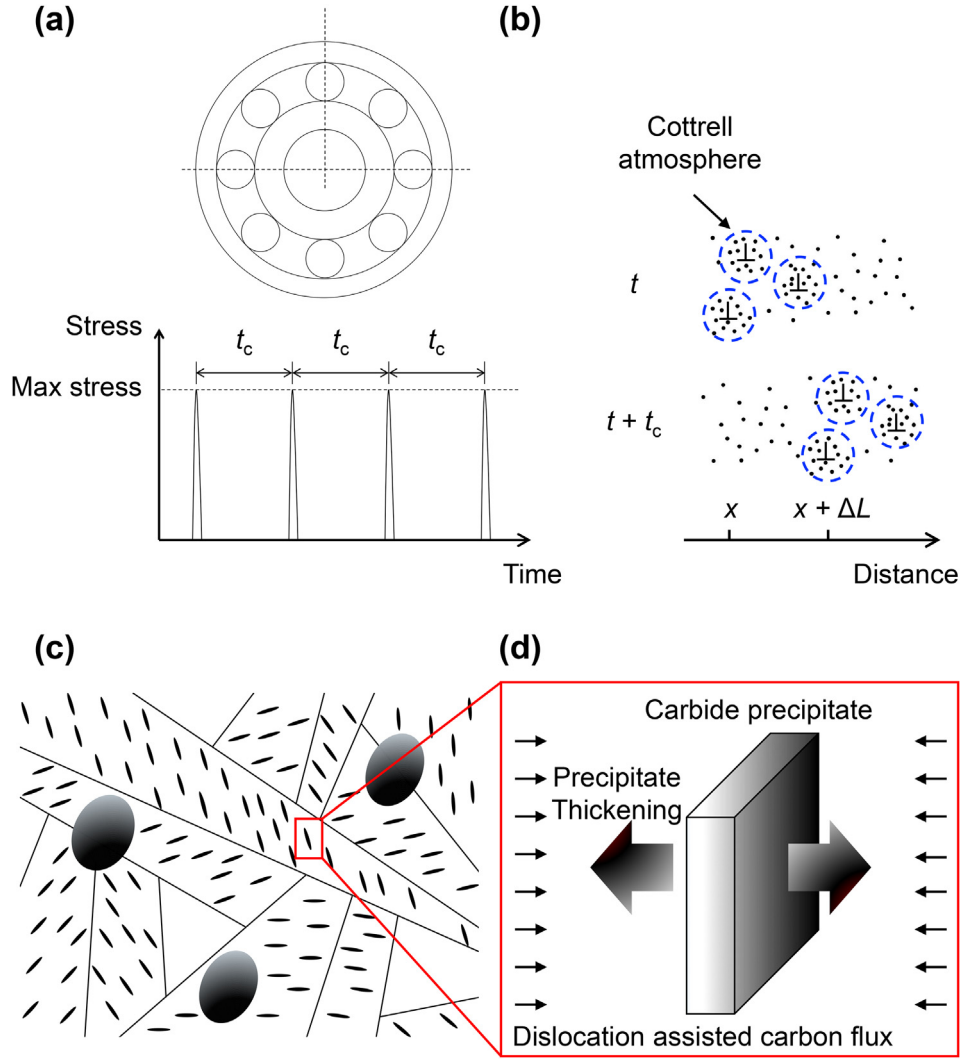
Fig. 2. Schematics showing the mechanism of dislocation assisted carbon migration towards pre-existing carbide precipitates during DER formation. (a) Stress history experienced by the bearing inner ring during bearing operation. (b) Cottrell atmospheres dragged by gliding dislocations within a stress cycle. (c) Microstructural of tempered martensite. (d) Thickening of a carbide precipitate by dislocation assisted carbon flux.

equilibrium can be obtained as:

$$\frac{dr_p}{dt}\left(C_{Vp} - C_{Vm}\right) = \frac{1}{2}\frac{\Delta\gamma\dot{N}}{b}\left[3\left(\frac{\pi}{2}\right)^{\frac{1}{3}}\left(\frac{AD}{kT\dot{N}}\right)^{\frac{2}{3}}C_{Vm}\right], \tag{2}$$

where t denotes the cycling time and C_{Vp} denotes the carbon concentration of the precipitate per unit volume. In Equation (2), the term on the left hand side represents the carbon flux of precipitate thickening while the term on the right hand side represents half of the dislocation-assisted carbon migration flux. Moreover, assuming the spacing between the precipitates to be l_p, a carbon mass conservation always holds for the studied system, given by:

$$l_p C_{V0} = 2r_p C_{Vp} + (l_p - 2r_p)C_{Vm}, \tag{3}$$

where C_{V0} is the initial carbon concentration of the system per unit volume. Equation (3) leads to the evolution of C_{Vm} as follows:

$$C_{Vm} = \frac{l_p C_{V0} - 2r_p C_{Vp}}{l_p - 2r_p}. \tag{4}$$

Equation (4) shows the carbon depletion in the matrix with

precipitate thickening. As a DER is a mixture of DER ferrite patches and parent martensite, the extent of martensite decay can be quantified by the area fraction of DER ferrite, termed DER%, which can be measured from optical microscopy. On the other hand, if assuming the decayed martensite (DER ferrite) is completely carbon depleted, the measured DER% is equivalent to the overall extent of carbon depletion in the matrix which can be calculated from the proposed model. This assumption is validated by the atom probe investigation in Section 5, where the carbon content in DER ferrite is measured to be as low as 0.02 at%, indicating that almost 99% of carbon has left the matrix. Hence DER% is given by:

$$DER\% = \frac{C_{V0} - C_{Vm}}{C_{V0}} \times 100\% \tag{5}$$

Furthermore, carbon depletion in the matrix leads to material

Table 1
Composition of 100Cr6 bearing steel (wt.%).

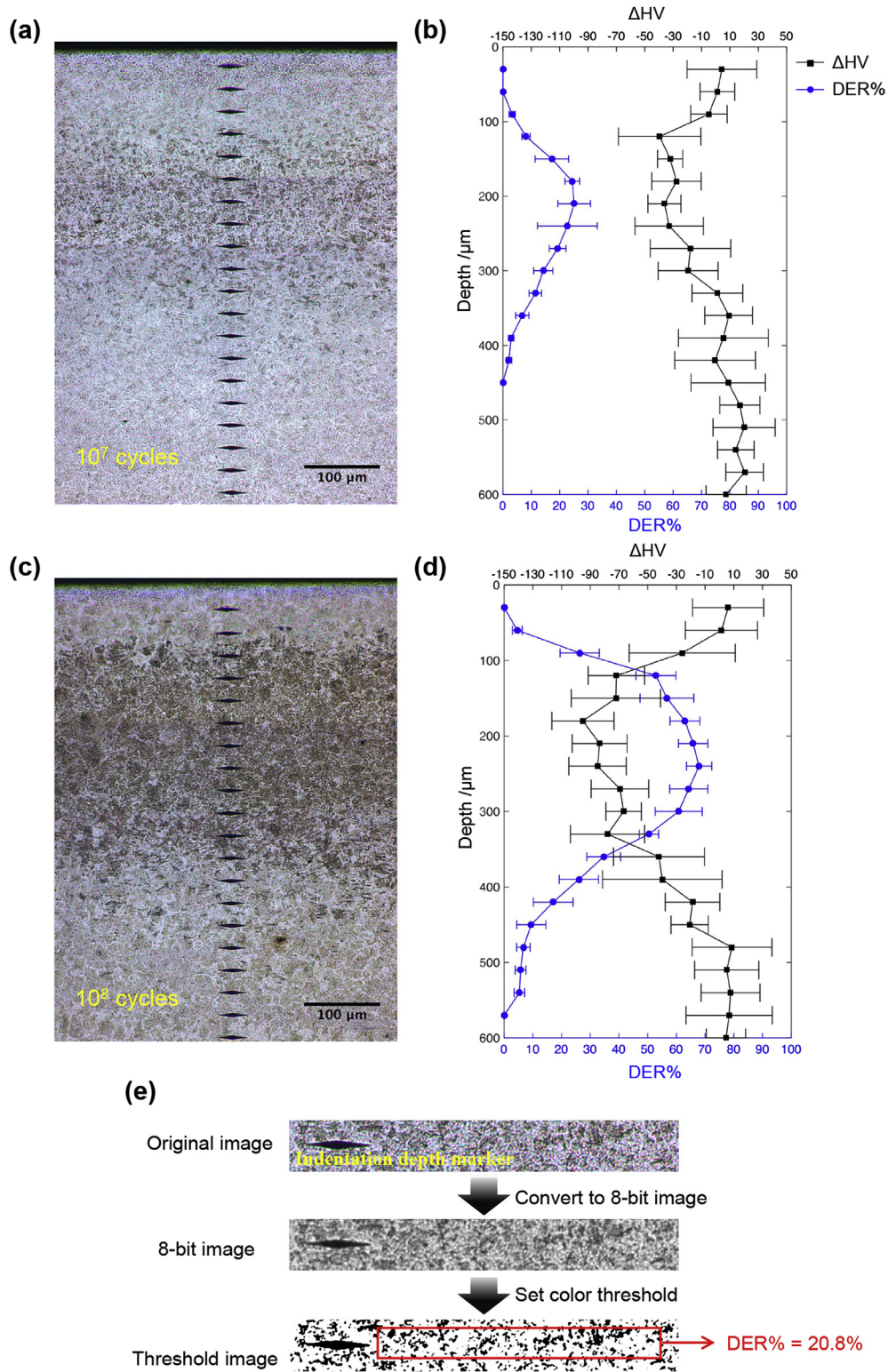| C	Cr	Mn	Si	Cu	Ni	Mo	Al
0.97	1.38	0.28	0.28	0.21	0.18	0.06	0.04

Fig. 3. (a) and (c) OM images of DERs formed in the circumferential sections of bearing inner rings run after 10^7 and 10^8 cycles, respectively. Rows of indents from microindentation tests are also shown. (b) and (d) Evolutions of DER% and ΔHV with respect to depth measured from the samples shown in (a) and (c). The error bars represent the standard deviation obtained from 6 repeated measures. (e) Illustration of the method to determine DER% at a certain depth from optical microscopy.

softening. According to the literature [5,6,8,10], the maximum hardness decrease in a fully formed DER is around 150 HV. Hence, following the rule of mixtures, the hardness change during DER formation can be estimated as:

$$\Delta HV = -150 \times DER\%. \tag{6}$$

3. Experimental validation

3.1. Material and RCF tests

Four through-hardened deep groove ball bearings of 6309 type were prepared for RCF tests. The material of the samples is 100Cr6 bearing steel. The composition of the material is listed in Table 1. The samples were first quenched from the austenitization condition at 830 °C and then tempered at 160 °C for 90 min, followed by air cooling to room temperature.

The RCF tests of the bearing samples were conducted on an SKF R2 RCF tester [27] under the same testing conditions for various predetermined number of cycles. The applied radial load was 25 kN, resulting in a maximum Hertzian contact pressure (p_0) of 3.2 GPa. The testing temperature was 83 °C, which was determined by measuring the outer ring temperature. The rotational speed of the tests was set to be 6000 rpm, giving a stress cycle frequency of 29760 cpm. The tests were suspended at 10^5, 10^6, 10^7, 10^8 cycles, respectively. The tested bearing inner ring samples were cut to show their axial and circumferential sections for further investigation.

3.2. Microindentation and microscopy

Microindentation and optical microscopy were carried out in the circumferential sections of the samples (Fig. 1 (a)). The surfaces were first ground with SiC papers to remove the deep scratches introduced by cutting, followed by polishing with 6 μm and 1 μm diamond paste to obtain a mirror finish. Finally, the surfaces were polished with 0.3 μm alumina suspension to remove the surface stress introduced during grinding and polishing. Microindentation tests were carried out using a Qness hardness tester, with indentation rows lying along the depth to study hardness evolution. In order to obtain detailed and accurate hardness evolving trends, a Knoop indentation tip was employed. For each test, the tip was loaded at 0.1 kg and held for 10 s before unloading. After the indentation, the computer automatically measured the long axis of the indent with a 650× optical microscope and calculated the hardness value, and then directly converted the result from HK0.1 to HV0.1. For each indentation row, the indents started from 30 μm below the surface and extended down to a depth of 600 μm, with the spacing between neighbouring indents being 30 μm. At least 6 indentation rows were repeated on each sample for averaging. After the microindentation tests, the samples were etched with 2% nital, which was considered to be the most efficient etchant to reveal DERs [14]. The indents can thus act as markers for depth below the contact surfaces. Optical microscopy was carried out

with a Leica optical microscope.

According to the experimental results, neither DERs nor significant hardness change was found in the samples run for 10^5 and 10^6 cycles, while the samples run for 10^7 and 10^8 cycles contain DERs with material softening detected. Fig. 3 (a) and (c) show optical images of the DERs formed at different stages of RCF. It can be seen that in general martensite decay becomes severer after a higher number of cycles. But it is worth noticing that in both samples, the distribution of DER ferrite patches is inhomogeneous and shows a significant variation with respect to depth.

As mentioned earlier, the extent of martensite decay can be quantified via DER%. Hence DER% at a certain depth is determined by optical microscopy analysis using the software ImageJ. An example is shown in Fig. 3 (e) to illustrate the procedure of the method. An optical image containing a section of a DER is magnified 200× with an indentation marker to pinpoint the depth; the image is then converted into an 8-bit image to obtain the contrast with gray scale; finally, an appropriate threshold is chosen based on the level of gray associated to dark patches from the parent martensite, and then a slice parallel to the marker is selected to calculate the area fraction of DER ferrite. It should be noted that during the metallographic investigation, the samples were slightly over-etched to make sure that all decayed martensite was revealed, and the threshold was chosen by varying this value until reaching a critical point below which the martensitic matrix (as reference) in the image was not extracted. This means that the calculated DER% can more precisely approach the actual DER fraction regardless of the extent of etching. The evolution of DER% and hardness change (ΔHV) with respect to depth are plotted for both samples as shown in Fig. 3 (b) and (d). It can be seen that DER% is related with the extent of material softening.

It is worth noticing that the variation of DER% along the depth is found to be comparable to the distribution of the orthogonal shear stress (τ_{yz}) in the bearing inner rings calculated from the Hertzian elastic contact theory [28], as shown in Fig. 4 (a). This eliminates the argument that DER formation is thermally induced [5,6], while there is strong evidence of DERs being stress-induced. It can be seen that τ_{yz} peaks at the subsurface with a value of $0.28p_0$, where the severest martensite decay occurs. Moreover, the depth range of DER formation, around 90−550 μm below the contact surfaces, can index a threshold of τ_{yz}, termed τ_{yz}^{th}, for the onset of DER formation. For the steel used in this research, $\tau_{yz}^{th} \approx 0.56$ GPa.

3.3. Modelling results
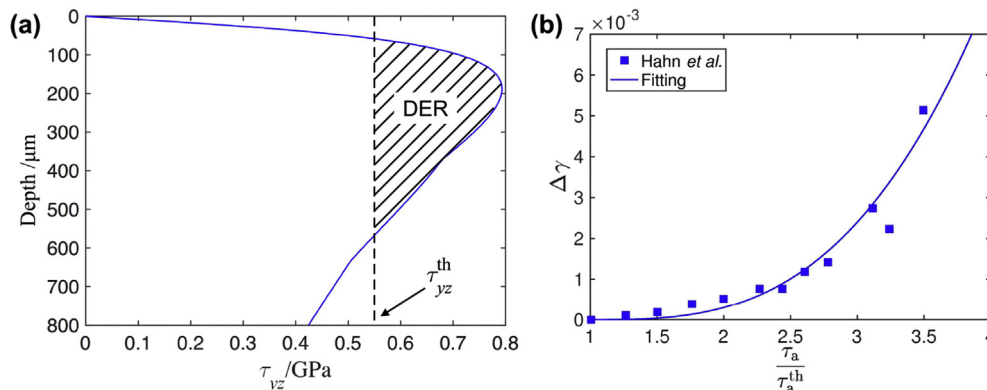
To carry out the calculation of the proposed DER formation

Fig. 4. (a) Comparison between the calculated τ_{yz} distribution along depth and the observed depth rang of DER formation. A threshold τ_{yz} for the onset of DER formation is indexed. (b) Plastic response of the steel determined from the cyclic torsion tests by Hahn et al. [29].

Table 2
Values of the constants used in the DER formation model.

Constant	Value
b	0.2876 nm
A	3×10^{-30} Nm^2 [34]
D_0	6.2×10^{-7} m^2 s^{-1}
E	80000 J mol^{-1} [35]
R	8.314 J K^{-1}mol^{-1}
k_B	1.38×10^{-23}m^2 kg s^{-2}K^{-1}

model, one key input, the plastic strain amplitude within each stress cycle, cannot be directly measured due to the complex stress state under rolling contact. Nevertheless, $\Delta\gamma$ can be obtained by referring to the traditional fatigue testing on the same steel. In this context, Hahn et al. [29] carried out cyclic torsion tests and measured the plastic response of the steel to applied shear stress. The experimental results indicate that the plastic strain amplitude increases exponentially with increasing load. Besides, it is generally thought [30] that $\Delta\gamma$ is a function of $\frac{\tau_a}{\tau_a^{th}} - 1$, where the ratio is between applied shear stress and threshold shear stress for the onset of plastic response. Therefore, the measured $\Delta\gamma$ from the cyclic torsion tests are plotted against $\frac{\tau_a}{\tau_a^{th}}$ in Fig. 4 (b), and an equation is obtained by fitting to the experimental data, being $\Delta\gamma = 0.0003\left(\frac{\tau_a}{\tau_a^{th}} - 1\right)^3$. Given that τ_{yz} is responsible for DER formation and following the same form of equation, the plastic response of the steel under RCF can be expressed as:

$$\Delta\gamma = 0.0003\left(\frac{\tau_{yz}}{\tau_{yz}^{th}} - 1\right)^3. \qquad (7)$$

Equation (7) describes the variation in material response along the depth when a Hertzian contact pressure is applied, and can

explain the inhomogeneous distribution of DER ferrite patches. Equations with a similar form were also employed in other RCF modelling work [31,32]. Other RCF testing conditions such as T and $\dot{N}$ can be directly obtained from the test setting.

As for the microstructural parameters, the average initial half width of the precipitates (r_{p0}) for the steel investigated in this research was estimated to be $\sim$7 nm, and the initial volume fraction of the precipitates (f_{p0}) was estimated to be $\sim$6.7 vol% [24]. Hence, the spacing between the precipitates can be approximated via $l_p = \frac{2r_{p0}}{f_{p0}}$ [19]. The total carbon content (C_0) of the system was calculated by Kang et al. [19] to be 3.1 at%, which can be converted to carbon concentration per unit volume through $C_{V0} = \frac{2C_0}{a_m^3}$, where a_m is the lattice parameter of body-centred cubic ferrite, equal to the magnitude of Burgers vector b. Besides, the carbon concentration within the precipitates, if assuming θ type carbides, is calculated via $C_{Vp} = \frac{4}{a_\theta b_\theta c_\theta}$, where a_θ, b_θ and c_θ are the lattice parameters of cementite equal to 0.452 nm, 0.509 nm and 0.674 nm, respectively [33]. The values of other constants used for the model are listed in Table 2.

Note D_0, the maximal diffusion coefficient for carbon, E, the activation energy for carbon diffusion, and R, the ideal gas constant are used to calculate carbon diffusivity in body-centred cubic iron at a certain temperature via $D = D_0\exp(-E/RT)$ [35].

By inputting the testing conditions, the material response, the microstructural parameters and the constants, and solving Equations (2) and (4)–(6), the distributions of DER% and ΔHV within a bearing inner ring after a given number of cycles can be predicted. Fig. 5 (a) and (b) show the modelling results in comparison to the experimental measurements on the samples shown in Fig. 3 (b) and (d). Good agreement is obtained.

Moreover, the proposed model is applied to predict the reported data under various RCF testing conditions from the literature. Note the steels used in the reported work have the same composition
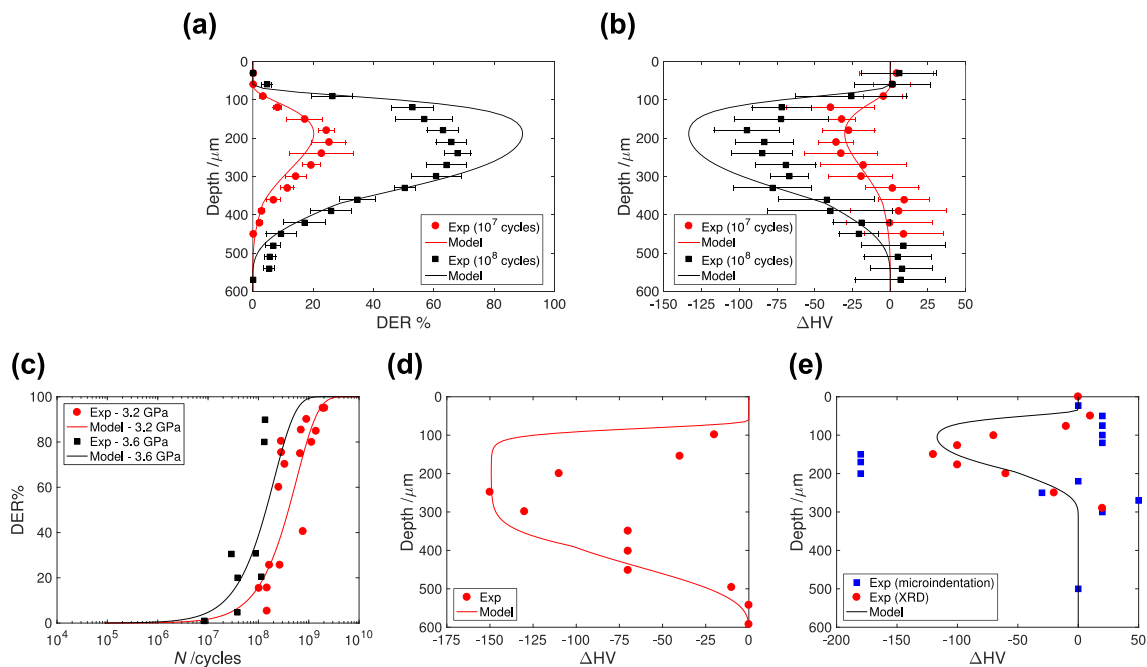

Fig. 5. (a) and (b) Comparison between the modelling results and the experimental data presented in this research. (a) Results for DER%. (b) Results for ΔHV. (c), (d), and (e) Comparison between the modelling results and the experimental data from the literature. (c) Results for DER% evolution with increasing number of cycle reported by Bush et al. [5]. (d) Results for ΔHV evolution along depth of a fatigued bearing inner ring reported by Lund [6]. (e) Results for ΔHV evolution along depth of a fatigued bearing inner ring reported by Bush et al. [5].

and heat treatment as in this research, and therefore the same material response to RCF and microstructural parameters are used for the calculations. In Fig. 5 (c), the evolution of DER% at the centre of DERs formed in the inner ring samples suspended at different number of cycles was reported by Bush et al. [5], who obtained the data using an optical microscopic method with the same principle as that presented in this research. The RCF tests were performed on 3208 type ball bearings with a rotational speed of 10640 cpm. The operation temperature was about 30 °C, and two contact pressures were employed, 3.2 and 3.6 GPa. The model makes good predictions for both cases. In Fig. 5 (d) and (e), predictions are made for the ΔHV evolution along depth. The sample in Fig. 5 (d), as reported by Lund [6], was a 6309 type ball bearing inner ring tested under 3.27 GPa with a rotational speed of 69760 cpm, and the operation temperature was 60 °C. The test was suspended after 10^9 cycles. The calculated ΔHV profile agrees with the measurements. The sample in Fig. 5 (e), as reported by Bush et al. [5], was a 3208 type ball bearing tested under 3.2 GPa with a rotational speed of 10640 cpm, and the operation temperature was 30 °C. The test was suspended at 1.2×10^9 cycles. Two sets of ΔHV data were obtained from the fatigued inner ring sample using microindentation and X-ray diffraction (XRD) microstress analysis. The measurements from the XRD tests exhibit smoother evolution, and the prediction curve agrees better with it.

4. Discussion

4.1. Parametric study

The comparison between modelling results and experimental data indicates that the proposed model can correctly describe the progress of DER formation under various testing conditions. Therefore, it is necessary to study how each condition affects DER formation and the cause behind it. The effects of three major factors, T, p_0 and $\dot{N}$ are presented in Fig. 6. Note that all the curves are calculated for the severest martensite decay. As shown in Fig. 6 (a), DER development is accelerated by increasing operation temperature. This is because DER formation is controlled by dislocation-assisted carbon migration and, under higher temperatures, according to Equation (2), carbon diffusivity is higher, and therefore more carbon can be captured by gliding dislocations within a stress cycle, resulting in a higher carbon flux. Higher stress levels, on the other hand, promote carbon flux indirectly through higher Δγ, which causes severer dislocation glide. Fig. 6 (b) shows the accelerated DER formation curves by increasing p_0. However, increasing rotational speed delays the formation of DERs, as shown in Fig. 6 (c). As t_c is inversely proportional to $\dot{N}$, higher $\dot{N}$ results in lower t_c, which causes less carbon to be captured by dislocations within a stress cycle, leading to a lower carbon flux. The predicted acceleration and deceleration effects of the testing conditions agree with the literature [2], and the proposed model can be used to quantify these effects.

4.2. DER% maps

The calculations in Fig. 6 imply that, under RCF testing, the effect of rotational speed on DER formation is less significant than that of the maximum contact pressure or temperature. In most cases, additionally, stress and temperature are of more interest from an industrial point of view [4,10]. Hence 3-dimensional maps of DER formation are shown for various p_0 and T values using the proposed model. In Fig. 7 (a), DER% maps are calculated for $N = 10^6, 10^7, 10^8$ and 10^9 cycles, where each surface represents a DER% map. The corresponding contour plots are shown in Fig. 7 (b), (c), (d) and (e),

and DER formation progress can thus be directly indexed for any given RCF testing conditions. These maps have a potential impact on the bearing industry as they can largely reduce the necessity of carrying out a great number of time-consuming full endurance tests under various testing conditions to study the microstructural alterations. Moreover, the DER% maps are a useful tool if combined
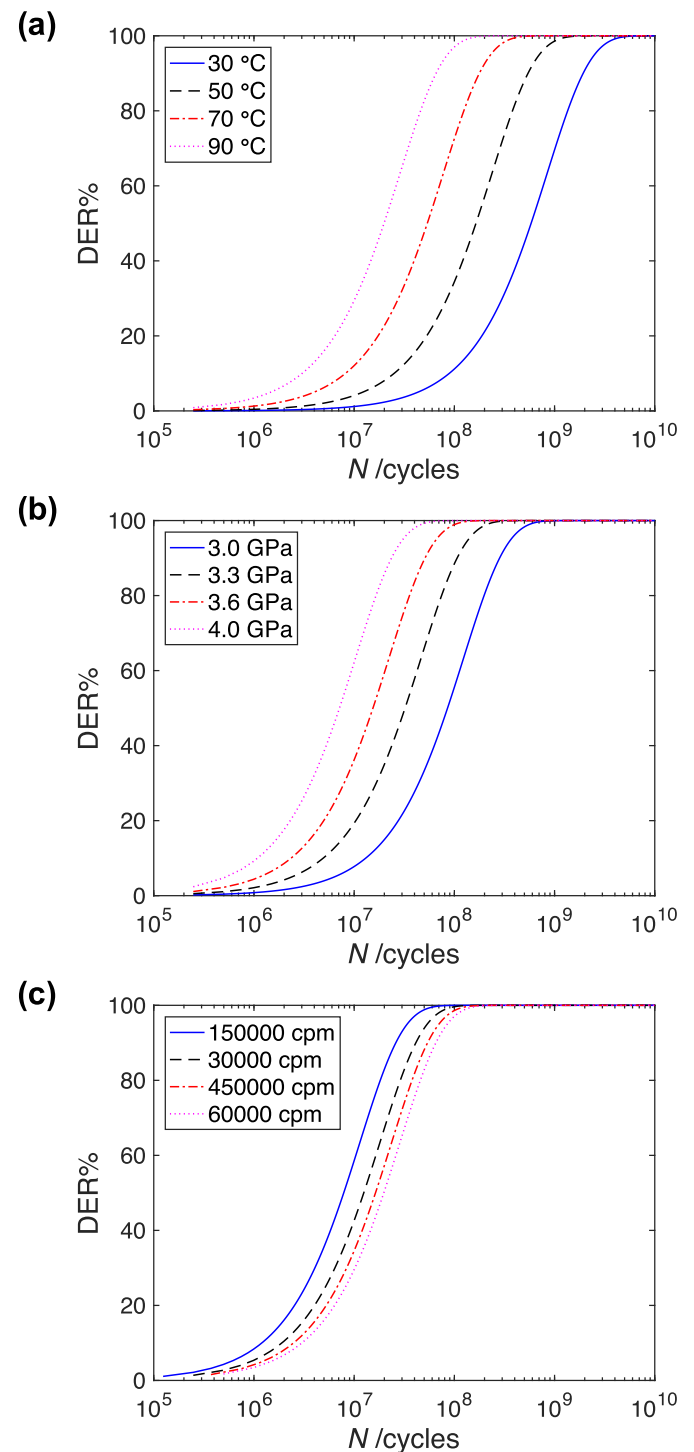

Fig. 6. Effects of RCF testing conditions on DER formation. (a) DER formation curves under increasing T with other conditions constant (p_0 = 3.3 GPa, $\dot{N}$ = 30000 cpm). (b) DER formation curves under increasing p_0 with other conditions constant (T = 80 °C, $\dot{N}$ = 30000 cpm). (c) DER formation curves under increasing $\dot{N}$ with other conditions constant (T = 80 °C, p_0 = 3.3 GPa).
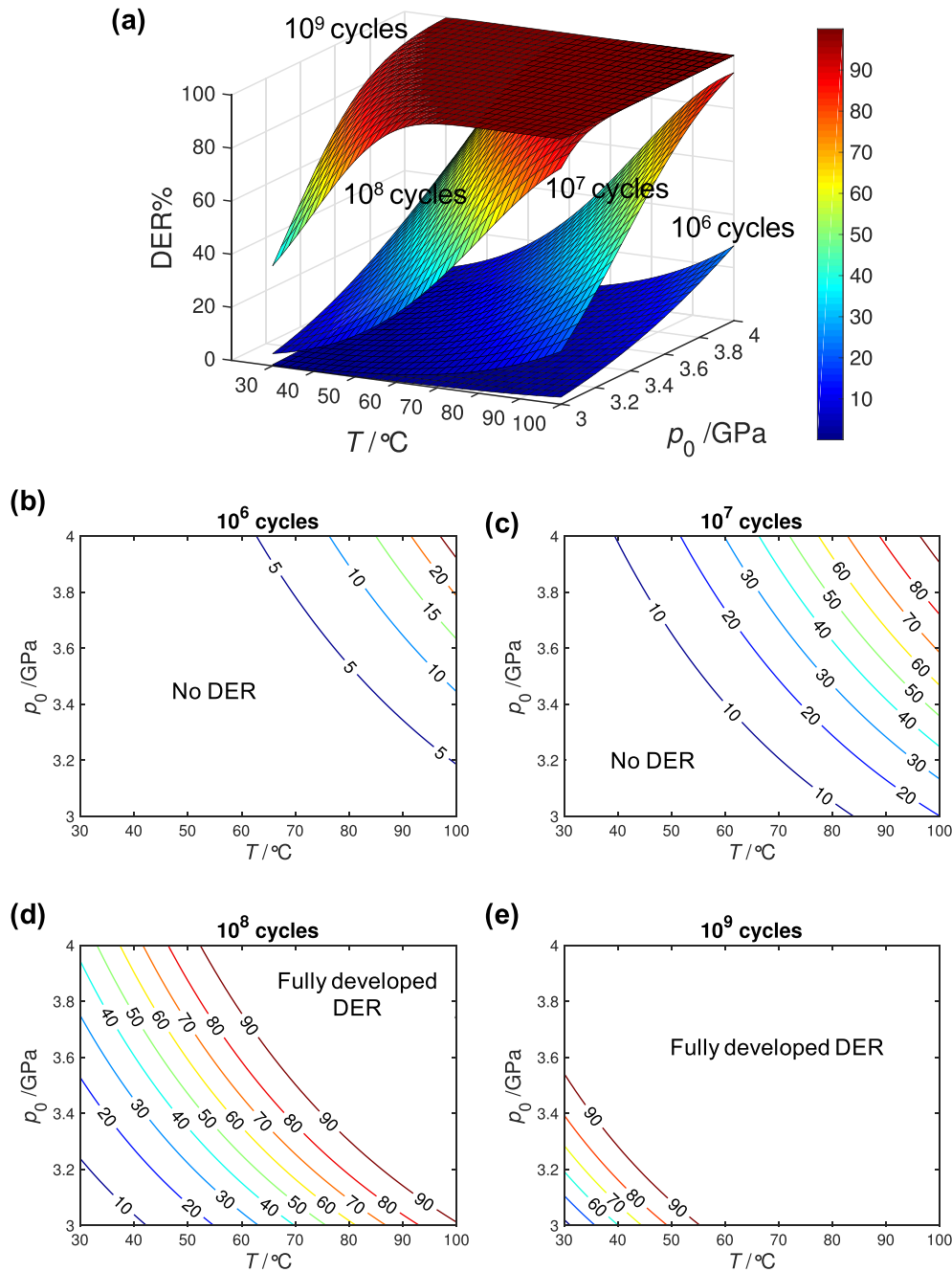
Fig. 7. Calculation of 3D DER% maps under various p_0 and T. (a) Maps calculated for N = 10^6, 10^7, 10^8 and 10^9 cycles. (b), (c), (d) and (e) Contour plots of the maps in (a).

with bearing fatigue life models, considering that crack propagation rate can definitely be altered by material softening [36].

5. Atom probe tomography

The proposed DER formation model suggests a strain-induced carbon migration mechanism. In other words, the redistribution of carbon in the matrix controls such martensite decay. In order to further study and visualise the behaviour of carbon during DER formation and to confirm the basic postulates in the model, an atom probe tomography (APT) test was carried on DER ferrite. Such atomic-scale characterisation can reveal the nature of DERs with

very high accuracy.

5.1. Experimental methods

Fig. 1 (c) is a secondary electron (SE) image of the DER formed in the sample run to 10^8 cycles taken from scanning electron microscopy (SEM). The image shows a part with the severest martensite decay. It is worth noticing that the DER ferrite patches display a light contrast to the parent martensite under SEM. The location from which the APT specimen was extracted is marked by the circle, inside DER ferrite. The APT specimen was cut and shaped by focused ion beam (FIB, FEI Helios NanoLab 660), and the APT
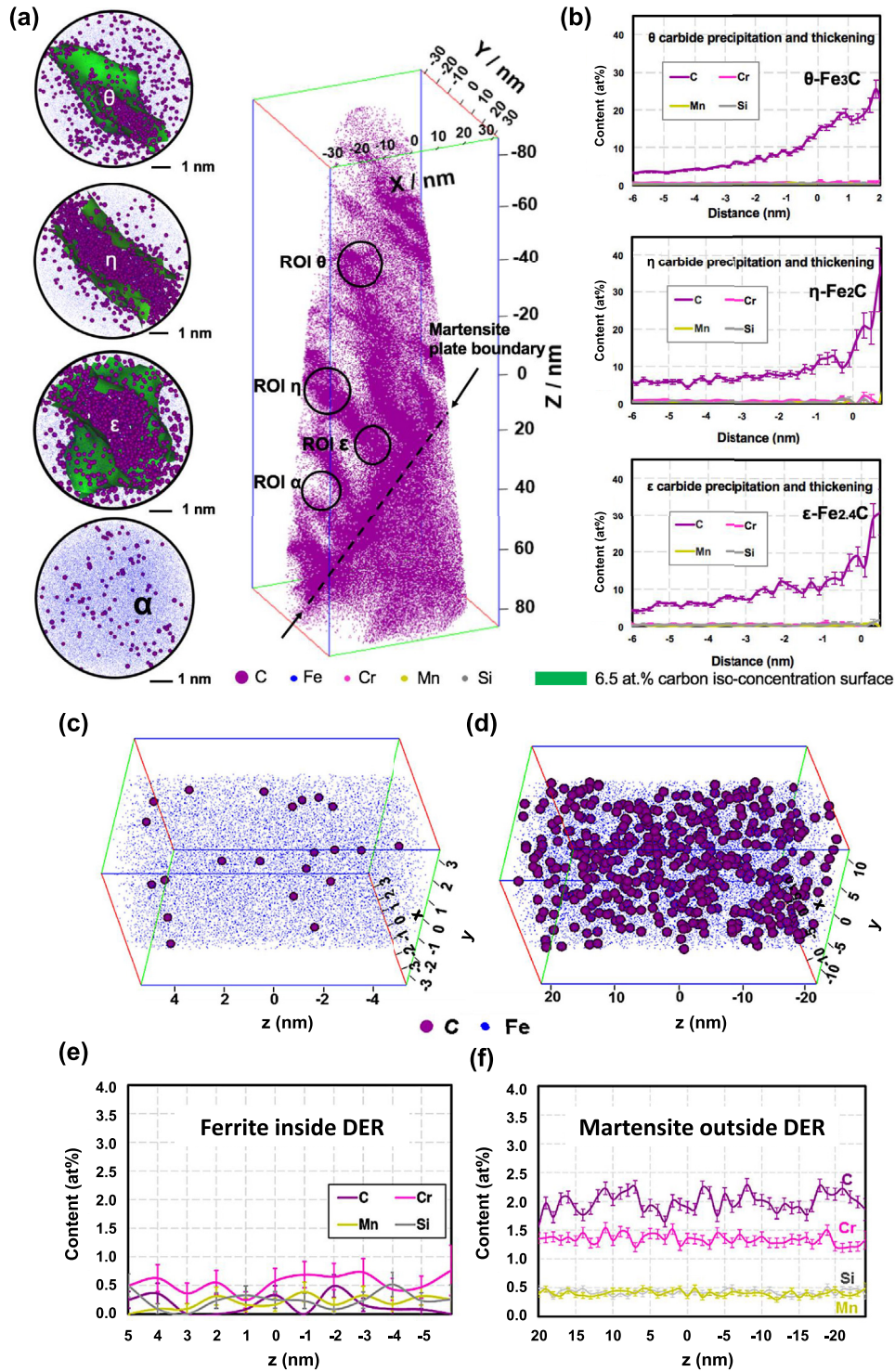
Fig. 8. APT characterisation of the APT specimen. (a) 3D atomic map with the analysis of different types of carbides (ε, η, θ) and DER ferrite and at the selected ROIs. (b) Proxigrams for the carbides selected in (a). (c) and (d) Comparison of the carbon distributions in DER ferrite and in parent martensite, respectively. The corresponding 1D content profiles of different alloying elements are plotted in (e) and (f).

analyses were performed using a Local Electrode Atom Probe (LEAP 4000X HR, Cameca Instruments) in pulsed voltage mode at a pulse fraction of 15% and a pulse frequency of 200 kHz. The specimen base temperature was about 60 K. The collected raw data were reconstructed into three-dimensional (3D) atomic maps and a precise decomposition process was conducted using IVAS software.

5.2. APT results and discussion

An overview of the atom distribution in the dark etching region for different alloying elements obtained from the APT analysis shows that C exhibits significant partition within the specimen whilst the other alloying elements such as Cr, Mn and Si are

homogeneously distributed. This implies that the formation of DERs is predominantly controlled by the redistribution of carbon.

A more detailed 3D atomic map in the DER is presented in Fig. 8 (a). The detection volume is $65 \times 65 \times 170$ nm^3. The non-homogeneous distribution of carbon is manifested by carbon enriched and depleted zones. It follows that the carbon depleted zones represent DER ferrite whilst the carbon enriched zones indicate nano-precipitates, e.g. θ, η and ε carbides. C is also enriched at the martensite plate boundary with a content of 6—7 at% as indicated by the arrows and the dashed line in Fig. 8 (a), agreeing with the saturation carbon content of Cottrell atmospheres [37,38]. Fig. 8 (a) shows examples of the element distribution in the precipitates selected and analysed at the regions of interest (ROIs), with the proxigrams for different ROIs shown in Fig. 8 (b). The particle with a carbon content of approximately 25 at% is identified as Fe$_3$C carbide (θ), that with a carbon content of approximately 33.3 at% as Fe$_2$C carbide (η) and that with a carbon content of approximately 29.4 at% as Fe$_{2.4}$C carbide (ε), owing to their respective stoichiometries. In total, over 15 carbon enriched zones are detected in the dataset, most of which are identified as θ. Nevertheless, the presence of transition carbides and the fact that they are surrounded by DER ferrite is strong evidence of carbon migration from the parent martensite towards pre-existing temper carbides, because ε and η carbides are formed during steel tempering [18,24]. This finding supports the fundamental postulate of the suggested DER formation mechanism.

To further confirm the carbon depletion during DER formation, a carbon atomic map in DER ferrite is presented in Fig. 8 (c), in comparison to the carbon distribution in parent martensite (Fig. 8 (d)). The corresponding 1D content profiles are plotted in Fig. 8 (e) and (f), respectively. For better visualisation, the carbon atoms are shown in 0.19 nm spheres and the iron atoms are shown as points. The average carbon content in the parent martensite is approximately 2.1 at%, whilst the carbon content in the DER ferrite is much lower, ranging within 0.02—0.6 at%. Beside, it is worth noticing that Cr content in the DER ferrite ($\sim$0.66 at%) is also lower than that in the parent martensite ($\sim$1.39 at%), which is probably due to the redistribution of Cr in the vicinity of the Cr-enriched globular carbides.

6. Conclusions

A DER formation model has been proposed on the basis of a dislocation-assisted carbon migration mechanism to describe strain-induced martensitic matrix decay in bearing steels under rolling contact fatigue. The proposed model takes into consideration testing conditions and microstructural parameters, and is capable of predicting the formation progress of DERs which is quantified by DER% and the corresponding evolution of hardness, ΔHV. The modelling results were compared with the experimental data from both this research and the literature, with good agreement obtained. The effects of RCF testing conditions on DER formation have been discussed. Moreover, 3D DER% maps are developed as a tool to index the progress of DER formation under various testing conditions.

This research also presents the first ever APT results of DERs in order to study the redistribution of carbon from the atomic scale. The results confirm carbon depletion in DER ferrite as predicted by the model. Moreover, various types of transition carbides were detected in DER ferrite, which strongly supports the postulate of the model that pre-existing carbide precipitates are carbon absorbers. Generally speaking, the APT results reveal the nature of DERs and confirm the suggested DER formation mechanism.

Future work is suggested to embed the DER formation model into bearing life models so that martensite decay is taken into account for crack propagation.

References

[1] H.K.D.H. Bhadeshia, Steels for bearings, Prog. Mater. Sci. 57 (2) (2012) 268—435.
[2] A. Warhadpande, F. Sadeghi, R.D. Evans, Microstructural alterations in bearing steels under rolling contact fatigue part 1 — historical overview, Tribology Trans. 56 (3) (2013) 349—358.
[3] J.-H. Kang, B. Hosseinkhani, P.E.J. Rivera-Díaz-del Castillo, Rolling contact fatigue in bearings: multiscale overview, Mater. Sci. Technol. 28 (1) (2012) 44—49.
[4] A.P. Voskamp, Microstructural stability and bearing performance, ASTM Special Technical Publication Issue 1419, Bearing Steel Technology, Phoenix, AZ; United States, 2002, pp. 443—456, 8 May 2001 through 10 May 2001.
[5] J.J. Bush, W.L. Grube, G.H. Robinson, Microstructural and residual stress changes in hardened steel due to rolling contact, Trans. ASM 54 (1961) 390—412.
[6] T. Lund, Structural alterations in fatigue-tested ball-bearing steel, Jemkonter A. 153 (1969) 337—343.
[7] H. Muro, N. Tsushima, Microstructural, microhardness and residual stress changes due to rolling contact, Wear 15 (5) (1970) 309—330.
[8] H. Swahn, P.C. Becker, O. Vingsbo, Martensite decay during rolling contact fatigue in ball bearings, Metall. Trans. A 7 (8) (1976) 1099—1110.
[9] H. Schlicht, Material properties adapted to the actual stressing in a rolling bearing, Ball Roller Bear. Eng. 1 (1981) 24—29.
[10] O. Zwirlein, H. Schlicht, Rolling contact fatigue mechanisms accelerated testing versus field performance, Rolling Contact Fatigue Test. Bear. Steels 771 (1982) 358—379.
[11] T. Ochi, Y. Kusano, Change in microstructure and properties in the rolling contact fatigue of bearing steel.
[12] A.B. Jones, Metallographic observations of ball bearing fatigue phenomena, in: Proc. ASTM, Vol. 46, Am. Soc. Testing and Materials New York, 1946, pp. 1—6.
[13] J.A. Martin, S.F. Borgese, A.D. Eberhardt, Microstructural alterations of rolling bearing steel undergoing cyclic stressing, J. Fluids Eng. 88 (3) (1966) 555—565.
[14] R. Österlund, O. Vingsbo, Phase changes in fatigued ball bearings, Metall. Trans. A 11 (5) (1980) 701—707.
[15] N. Mitamura, H. Hidaka, S. Takaki, Microstructural development in bearing steel during rolling contact fatigue, Mater. Sci. Forum 539 (2007) 4255—4260.
[16] W.F. Smith, J. Hashemi, Foundations of Materials Science and Engineering, McGraw-Hill, 2011.
[17] J. Buchwald, R.W. Heckel, An analysis of microstructural changes in 52100 steel bearings during cyclic stressing (microstructural changes in 52100 steel bearing inner rings during cyclic stressing, obtaining thickening rate data on white-etching regions and lenticular carbides), ASM Trans. Q. 61 (1968) 750—756.
[18] G.R. Speich, W.C. Leslie, Tempering of steel, Metall. Mater. Trans. B 3 (5) (1972) 1043—1054.
[19] J.H. Kang, B. Hosseinkhani, R.H. Vegter, P.E.J. Rivera-Díaz-del Castillo, Modelling dislocation assisted tempering during rolling contact fatigue in bearing steels, Int. J. Fatigue 75 (2015) 115—125.
[20] J.M. Beswick, Measurement of carbon levels in structurally transformed SAE 52100 ball bearing steel by microprobe analysis, Pract. Metallogr. 12 (1975) 200—206.
[21] H. Fu, E. Galindo-Nava, P.E.J. Rivera-Díaz-del Castillo, Modelling and characterisation of stress-induced carbide precipitation in bearing steels under rolling contact fatigue, Acta Mater. 128 (2017) 176—187.
[22] J.H. Kang, B. Hosseinkhani, C.A. Williams, M.P. Moody, P.A.J. Bagot, P.E.J. Rivera-Díaz-del Castillo, Solute redistribution in the nanocrystalline structure formed in bearing steels, Scr. Mater. 69 (8) (2013) 630—633.
[23] Y.J. Li, M. Herbig, S. Goto, D. Raabe, Atomic scale characterization of white etching area and its adjacent matrix in a martensitic 100Cr6 bearing steel, Mater. Charact. 123 (2017) 349—353.
[24] A.T.W. Barrow, J.H. Kang, P.E.J. Rivera-Díaz-del Castillo, The $\varepsilon \to \eta \to \theta$ transition in 100Cr6 and its effect on mechanical properties, Acta Mater. 60 (6) (2012) 2805—2815.
[25] A.P. Voskamp, Material response to rolling contact loading, J. Tribology 107 (3) (1985) 359—364.
[26] A.T.W. Barrow, P.E.J. Rivera-Díaz-del Castillo, Nanoprecipitation in bearing steels, Acta Mater. 59 (19) (2011) 7155—7167.
[27] M. Ragen, G. Zimmerman, Rolling contact fatigue strength testing and material developments in aerospace bearings a retrospective analysis, in: Bearing Steel Technologies: 9th Volume, Advances in Rolling Contact Fatigue Strength Testing and Related Substitute Technologies, ASTM International, 2012.

[28] A. Sackfield, D.A. Hills, D. Nowell, Mechanics of Elastic Contacts, Elsevier, 2013.

[29] G.T. Hahn, V. Bhargava, Q. Chen, The cyclic stress-strain properties, hysteresis loop shape, and kinematic hardening of two high-strength bearing steels, Metall. Trans. A 21 (2) (1990) 653–665.

[30] A.F. Bower, K.L. Johnson, The influence of strain hardening on cumulative plastic deformation in rolling and sliding line contact, J. Mech. Phys. Solids 37 (4) (1989) 471–493.

[31] A. Kapoor, F.J. Franklin, Tribological layers and the wear of ductile materials, Wear 245 (1) (2000) 204–215.

[32] F.J. Franklin, I. Widiyarta, A. Kapoor, Computer simulation of wear and rolling contact fatigue, Wear 251 (1) (2001) 949–955.

[33] G. Krauss, Steels: Processing, Structure, and Performance, ASTM International, 2015.

[34] A.H. Cottrell, B.A. Bilby, Dislocation theory of yielding and strain ageing of iron, Proc. Phys. Soc. Sect. A 62 (1) (1949) 49.

[35] H.K.D.H. Bhadeshia, R. Honeycombe, Steels: Microstructure and Properties, Butterworth-Heinemann, 2011.

[36] H. Homma, H. Nakazawa, Effect of mechanical properties of material on rate of fatigue crack propagation, Eng. Fract. Mech. 10 (3) (1978) 539–552.

[37] J. Wilde, A. Cerezo, G.D.W. Smith, Three-dimensional atomic-scale mapping of a Cottrell atmosphere around a dislocation in iron, Scr. Mater. 43 (1) (2000) 39–48.

[38] D.H. Sherman, S.M. Cross, S. Kim, F. Grandjean, G.J. Long, M.K. Miller, Characterization of the carbon and retained austenite distributions in martensitic medium carbon, high silicon steel, Metall. Mater. Trans. A 38 (8) (2007) 1698–1711.